Supporting Information

A linear scaling relation for CO oxidation on CeO_2-supported Pd

Jin-Xun Liu, Yaqiong Su, Ivo A.W. Filot and Emiel J.M. Hensen*

Inorganic Materials Chemistry, Department of Chemistry and Chemical Engineering, Eindhoven University of Technology, Eindhoven, 5600 MB, Netherlands

* Correspondence to: e.j.m.hensen@tue.nl (EJMH)

Calculation methodology details

DFT calculations

All spin-polarized DFT calculations were performed using the Vienna ab initio simulation package (VASP) code.[1,2] The projector augmented wave (PAW)[3] potentials and Perdew–Burke–Ernzerhof (PBE) functionals were adopted.[4] For all DFT calculations, Brillouin zone sampling was restricted to the Γ point. The energy cut off of the plane wave basis set was 300 eV for structure optimization and the convergence threshold for geometry optimization was set to 10^{-4} eV. Geometry optimization was deemed converged when the forces on each atom were below 0.05 eV/Å. To properly account for electron localization in Ce *4f*-orbitals, the DFT+U method with U_{eff} = 5 eV was employed. A genetic algorithm (GA) approach based on the Deaven-Ho scheme using DFT to compute the energies of candidate structures was employed. This approach was used to find global minimum structures of Pd_8 in the gas phase and adsorbed on stoichiometric and defective CeO_2(111) surfaces. A *p*(3×3) CeO_2(111) surface with two O-Ce-O layers was used as a support model. The six most stable structures identified by GA were once more optimized with a kinetic energy cut off of 400 eV while also relaxing the other O-Ce-O layers except the bottom one. For the grand-canonical Monte Carlo calculations we used a *p*(4×4) CeO_2(111) surface cell. Neighboring slabs were separated by a vacuum of 15 Å to avoid self-interactions.

RPBE potentials were used to obtain accurate adsorption energies of the intermediates for determination of the CO oxidation cycle.[5] The plane-wave basis with a cut off energy of 400 eV was used, employing the +U correction with U_{eff} = 5 for Ce.[6] For Pd_8, all the atoms were allowed to relax in a 15 Å × 15 Å × 15 Å box. Calculations of the supported and unsupported Pd_8 nanoparticle were performed in the Γ-point. The top O-Ce-O layer and adsorbates were relaxed for the periodic ceria-supported Pd_8 nanoparticles. The climbing-image nudged elastic band (CI-NEB) method was used to locate the transition state for CO oxidation with a force tolerance of 0.05 eV/Å.[7,8] Vibrational mode analysis was done to verify the identified transition states.

Genetic algorithm (GA) calculations

GA-DFT calculations have been conducted to find the global minimum structures of Pd_8, perfect and defective CeO_2 (111) supported Pd_8 nanoclusters. The first step for GA run is to generate the initial population (12 random starting candidates used here) randomly. All the starting candidates should be reasonable with the bond distances in the region of 2 Å ~ 3Å avoiding redundant calculations. Then, DFT calculations have been performed to calculate the energy of each structure. During the GA-DFT calculations, the relative energies and sorted distance matrices are used to judge whether the two candidates have the same structures. The calculated energies of the structures are used in the assigning of the fitness

and the structures with lower energy have higher possibility to be maintained in the population. The fitness function of i^{th} candidate (F_i) can be calculated as below[9]:

$$F_i = ½[1-\tanh(2\rho_i-1)] \text{ with } \rho_i = (E_i - E_{min})/(E_{max} - E_{min}) \quad (1)$$

E_{max} and E_{min} is the maximum and minimum energy of any structure in the population.

After assigning the fitness, we generate new population by crossover, as introduced by Deaven and Ho,[10,11] and mutation operations which are the most important and key operators in GA. For crossover operation, we first choose two random cutting planes (m1 and m2) and position it in the common center of father structure C1 and structure C2, respectively. By generating new structure, we select all atoms from C1 which are to the left of the plane m1 and all atoms from the structure C2 which are to the right of the plane m2. If the total number of new structure (N_n) is larger than N, we remove the N_n-N atoms which are farthest away of the new structure. However, if $N_n < N$, we randomly chose N-N_n atoms from C2 which were not previously included. The generated new structure should have reasonable bond distances and be different with other structures in the population.

For the mutation operation in GA, the rattle and twist operation are considered. Firstly, 40% atoms in transition metal clusters are allowed to move a random distance in a random direction with the perturbations between -0.6 Å and 0.6 Å. Then, the adsorbed cluster can be rotated a random angle ranging from 1° – 180° with respect to the surface normal. After the mutation operation, we have to confirm the new generated structures are reasonable with suitable bonds distances. The random number is generated by Mersenne Twister random number generator.

The above steps are cycled to optimize and generate more and more populations. More than 500 structures have been calculated and no new structure are obtained after 50 cycles. By using this GA methods, we can search the global minimum structure of Pd_8 and CeO_2 supported Pd_8 nanocluster.

Grand-canonical Monte Carlo (GCMC) simulations

GCMC simulation is an efficient approach to determine the properties of an adsorption phase or the stability of the structure in equilibrium with an infinite reservoir of ideal gas. In the present work, GCMC-DFT calculations have been conducted to search the most stable structure of Pd_8/CeO_2 catalyst under the oxygen atmosphere at specified temperature (300 K). Specifically, the principle of GCMC method is that the formation of Pd_8O_x/CeO_2 is in equilibrium with the O_2 gas in an imaginary reservoir. GCMC operates in the constant μVT ensemble. The chemical potential of O_2 in the gas phase and temperature (300 K) are the

input parameters for GCMC calculations. The chemical potential energy of the Pd_8O_x/CeO_2 structures at specified conditions can be written as below:

$$\mu(T, P) = E(Pd_8O_x/CeO_2) + [\mu_{O2\_reservoir} - x/2\mu_{O2}(T, P)] \quad (2)$$

Here, $\mu_{O2\_reservoir}$ is the chemical potential of oxygen reservoir. Whilst the chemical potential of single O_2 molecule in the gas phase ($\mu_{O2}(T, P)$) can be calculated as:

$$\mu_{O2}(T, P) = E_{O2} + \mu_{O2}(0, P_0) + kT\ln(P/P_0) \quad (3)$$

Where E_{O2} is energy of O_2 obtained by DFT calculations, $\mu_{O2}(0, P_0) = \Delta H\text{-}T\Delta S$ can be obtained from JANAF Table.[12]

In the GCMC simulations, addition, deletion and randomly movement of oxygen atoms are performed. For the present work, 25% of all the atoms in Pd_8O_x clusters are allowed to randomly move when doing the movement operations. The chemical potential of the ensemble is calculated after each trials (addition, deletion or movement). Metropolis algorithm is used to judge whether the present trial treatment is accepted or rejected.[13,14] From state with chemical potential μ_{n-1} to state with chemical potential μ_n by adding, deleting or randomly displacing oxygen atoms obey the following rule:

If $\mu_n < \mu_{n-1}$ … accept trial

If $\mu_n > \mu_{n-1}$ … generate a random number R,

$0 < R < 1$,

if $R < \exp(-(\mu_n-\mu_{n-1})/kT)$ …accept trial

if $R > \exp(-(\mu_n-\mu_{n-1})/kT)$ …reject trial and return to the old structure

The GCMC approach simulates the chemical equilibrium reached between a fictitious oxygen reservoir and Pd_8O_x/CO_2. At the equilibrium state, any addition, deletion or movement of oxygen will increase the chemical potential energy of the system. After 500 trials, no more new structures of Pd_8O_x/CO_2 will be generated at specified conditions and the final structure is considered as the most stable one searched by GCMC. An additional GCMC-DFT simulation showed that O vacancies are always rapidly healed in an O_2 atmosphere. This is the expected result as the O vacancy formation energy is higher than 2 eV. For our expensive GA-DFT and GCMC_DFT-calculations, we make one important assumption that the support does not change its shape.

Microkinetics simulations

The computed reaction barriers were used to compute the forward and backward reaction rate constants for CO oxidation. For the surface reactions, the rate constants for the forward and backward elementary reaction were determined by the Eyring equation[15]

$$k = Ae^{\frac{Ea}{k_b T}} \tag{4}$$

where k is the reaction rate constant in s^{-1}. In the prefactor $A = \frac{k_b T}{h}\frac{Q^{TS}}{Q}$, k_b, T, h and E_a are the Boltzmann constant, temperature, Planck's constant and the activation barrier, respectively. Q^{TS} and Q refer the partition functions of the transition and ground states, respectively. As an approximation, the pre-factor $A = \frac{k_b T}{h}\frac{Q^{TS}}{Q}$ is set to 10^{13} s^{-1} for all the elementary surface reactions.

For non-activated molecular adsorption, the rate of adsorption is determined by the rate of surface impingement of gas-phase molecules. Based on the Hertz-Knudsen equation,[16] we obtainthe molecular adsorption rate constant as:

$$k_{ads} = \frac{PA'}{\sqrt{2\pi m k_b T}} S \tag{5}$$

with P the partial pressure of the adsorbate in the gas phase, A' the surface area of the adsorption site, m the mass of the adsorbate and S the sticking coefficient.

For the desorption process, it is assumed that there are three rotational degrees of freedom and two translational degrees of freedom in the transition state. Accordingly, the rate of desorption is given by

$$k_{des} = \frac{k_b T^3}{h^3}\frac{A'(2\pi k_b)}{\sigma\theta_{rot}} e^{-\frac{E_{des}}{k_b T}} \tag{6}$$

where σ and θ are the symmetry number and the characteristic temperature for rotation, respectively. E_{des} is the desorption energy.

The approach to microkinetics simulations has been presented in detail elsewhere.[17,18] Differential equations for all the surface reaction intermediates were constructed using the rate constants and the set of elementary reaction steps. For each of the M components in the kinetic network, a single differential equation in the form

$$r_i = \sum_{j=1}^{N}\left(k_j v_i^j \prod_{k=1}^{M} c_k^{v_k^j}\right) \tag{7}$$

is obtained. In this equation, k_j is the elementary reaction rate constant (see equation 1), ν_i^j is the stoichiometric coefficient of component *i* in elementary reaction step *k* and c_k is the concentration of component *k* on the catalytic surface. The CO oxidation rate is calculated by the in-house developed MKMCXX program.[17-19] Steady-state coverages were calculated by integrating the ordinary differential equations in time until the changes in the surface coverages were very small. Because chemical systems typically give rise to stiff sets of ODEs, we have used the backward differentiation formula method for the time integration.[18] The rates of the individual elementary reaction steps were obtained based on the computed steady-state surface coverages. In our simulations, the gas phase consisted of CO and O_2 in 1:5 molar ratio at a total pressure of 40 Torr, which is close to typical experimental reaction conditions.[20] For CO oxidation on Pd_8/CeO_2, microkinetics simulations were conducted using a dual-site model. The surface area ratio of Pd_8 nanoparticles and CeO_2 support was set to 1/3. The reported coverages of the corresponding intermediates are normalized to these surfaces. The elementary reaction steps that contribute to the rate control over the overall reaction can be determined by degree of rate control (DRC) concept introduced by Campbell et al.[21-23] For elementary step *i*, the degree of rate control $X_{RC,i}$ can be defined as

$$X_{\mathrm{RC},i} = \frac{k_i}{r}\left(\frac{\partial r}{\partial k_i}\right)_{k_{j\neq i},K_i} = \left(\frac{\partial \ln r}{\partial \ln k_i}\right)_{k_{j\neq i},K_i} \tag{8}$$

where k_i, K_i and *r* are the rate constants, the equilibrium constant for step *i* and the reaction rate, respectively.

The dual-site microkinetics simulations were conducted for CO oxidation on $Pd_8(O_x)/CeO_2$ structures. Herein, there are two types of active sites as present on the $Pd_8(O_x)/CeO_2$ structures, i.e. active sites on $Pd_8(O_x)$ clusters or on the CeO_2 support. In our dual-site microkinetics simulations, CO adsorbs on $Pd_8(O_x)$ clusters (CO_{Pd}). Whereas O_2 adsorbs at the oxygen vacancy site (O_{2Ce}), CO_2 formation occurs at the interface of the $Pd_8(O_x)$ nanoparticles and the CeO_2 support. For the alternative scenario, O_2 molecule dissociates at the interface of $Pd_8(O_x)/CeO_2$ structures ($O_{2Ce} \rightarrow O_{Ce} + O_{Pd}$) and the dissociated O_{Pd} atom can be removed by $CO_{Pd} + O_{Pd} \rightarrow CO_2$ occurring on the $Pd_8(O_x)$ clusters. The migration of O atoms between the sites of $Pd_8(O_x)$ and CeO_2 is explicitly taken into account and the calculated reaction barriers are shown in Table S2. In the dual site microkinetics model, the active site ratio of 1:3, 1:2 and 1:5 are studied for the $Pd_8(O_x)$: CeO_2 and the corresponding CO oxidation rates on various structures are presented in Figure S5.

Pd loading on CeO_2 of the computational model

In our model, the Pd_8 nanoparticle is positioned on a $p(3\times3)$ CeO_2 support with a surface area S_1. The loading of one Pd_8 nanoparticle on CeO_2 can be calculated as:

$$L_1 = M_{Pd} / S_1$$

A typical CeO_2 surface area is S_{CeO2} = 50 m^2/g. Accordingly, the Pd loading can be approximated

$$L = M_{Pd}/S1 * 1/S_{CeO2} \approx 10 \text{ wt\%}$$

Table S1. The binding energy (in eV) of CO and O on $Pd_8(O_x)$ nanocluster and CeO_2 support, respectively. The activation barriers (E_a, in eV) for CO + O → CO_2 at the interface are also indicated.

Structures	E_{CO}	E_O	E_a
Pd_8/CeO_2	-1.86	-5.11	1.53
Pd_8/CeO_{2-x}	-1.81	-4.81	1.36
$Pd_8/CeO_{2-x'}$	-1.76	-5.05	1.43
Pd_8O_6/CeO_2	-1.60	-4.94	1.36
Pd_8O_{12}/CeO_2	-1.09	-4.96	0.83

Table S2. The calculated forward (E_f, in eV) and backward (E_b, in eV) reaction barriers for O migration from CeO_2 support to $Pd_8(O_x)$ cluster. These computed reaction barriers are considered in the microkinetics simulations.

Structures	E_f	E_b
Pd_8/CeO_2	1.71	0.55
Pd_8/CeO_{2-x}	1.29	0.08
$Pd_8/CeO_{2-x'}$	1.45	0.11
Pd_8O_6/CeO_2	1.23	0.81
Pd_8O_{12}/CeO_2	1.67	0.06

Table S3. Calculated the single negative imaginary frequencies (in cm^{-1}) for all the transition states for the elementary reaction steps involved in CO oxidation.

Structures	$CO_{Pd} + O_{2,ceria} \rightarrow CO_2 + O_{ceria}$	$CO_{Pd} + O_{ceria} \rightarrow CO_2$	$O_{2,ceria} \rightarrow O_{ceria} + O_{Pd}$	$CO_{Pd} + O_{Pd} \rightarrow CO_2$
Pd_8/CeO_2	178 i	314 i	410 i	382 i
Pd_8/CeO_{2-x}	156 i	277 i	379 i	345 i
$Pd_8/CeO_{2-x'}$	229 i	300 i	414 i	383 i
Pd_8O_6/CeO_2	482 i	359 i	450 i	339 i
Pd_8O_{12}/CeO_2	129 i	284 i	384 i	415 i

Table S4. The binding energies of CO (E_{CO}) and O_2 (E_{O2}) on the Pd_8O_x cluster and the oxygen vacancy sites in CeO_2, respectively. The oxygen vacancy energies (E_v) with respect to O_2 in the gas phase are also indicated. All the energies are given in eV.

Structures	E_{CO}	E_{O2}	E_V
Pd_8/CeO_2	-1.86	-1.95	2.23
Pd_8/CeO_{2-x}	-1.81	-1.39	1.97
$Pd_8/CeO_{2-x'}$	-1.76	-1.63	2.21
Pd_8O_6/CeO_2	-1.60	-1.49	2.12
Pd_8O_{12}/CeO_2	-1.09	-1.63	2.10

Table S5. Calculated TOF (s^{-1}) for CO oxidation at 323 K over $Pd_8(O_x)/CeO_2$ structures by microkinetics simulations.

Structures	TOF[a] (s^{-1})
Pd_8/CeO_2	6.3×10^{-12}
Pd_8/CeO_{2-x}	1.5×10^{-9}
$Pd_8/CeO_{2-x'}$	1.8×10^{-10}
Pd_8O_6/CeO_2	2.5×10^{-9}
Pd_8O_{12}/CeO_2	0.53

[a] In our simulations, the gas phase consisted of CO and O_2 in 1:5 molar ratio at a total pressure of 40 Torr, which is close to typical experimental reaction conditions.[20]

Table S6. Calculated TOF (s^{-1}) for CO oxidation at 293 K, 333 K and 413 K over Pd_8O_{12}/CeO_2 structures by microkinetics simulations.

Temperature	Calculated TOF[a] (s^{-1})	Experimental TOF (s^{-1})
293	0.0038	0.024[24]
323	0.53	0.02[25]
323	0.53	0.074[26]

[a] In our simulations, the gas phase consisted of CO and O_2 in 1:5 molar ratio at a total pressure of 40 Torr, which is close to typical experimental reaction conditions.[20]

Table S7. Comparison of CO adsorption energies (E_{CO}) and reaction barrier (E_a) for the rate-determining step (CO_{Pd} + O_{ceria} → CO_2) at the interface of Pd_8/CeO_2 and Pd_8O_{12}/CeO_2 structures by employing the computational settings in our work (*k*-points: Γ point and force convergence: 0.05 eV/Å) and the suggested more accurate settings (*k*-points: 2 x 2 x 1 and force convergence: 0.03 eV/Å). All the energies in eV.

Structures	E_{CO} Settings in this work	E_{CO} More accurate settings	E_a Settings in this work	E_a More accurate settings
Pd_8/CeO_2	-1.86	-1.90	1.53	1.56
Pd_8O_{12}/CeO_2	-1.09	-1.11	0.83	0.85

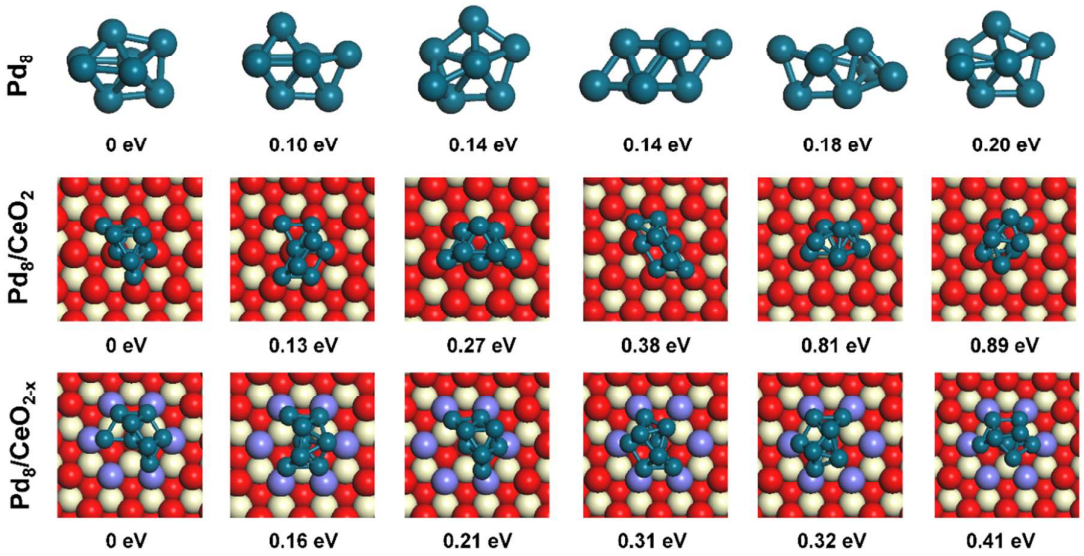

Figure S1. Structures of the candidates for the lowest-energy of Pd_8, Pd_8/CeO_2 and Pd_8/CeO_{2-x} structures searched by genetic algorithm based on DFT calculations. The energy values (in eV) beneath each isomers are the relative energy with respect to the lowest-lying one. The cyan, red, light yellow spheres represent Pd, O and Ce atoms. The purple spheres are the O atoms around the oxygen vacancy site. This notation is used throughout this SI file.

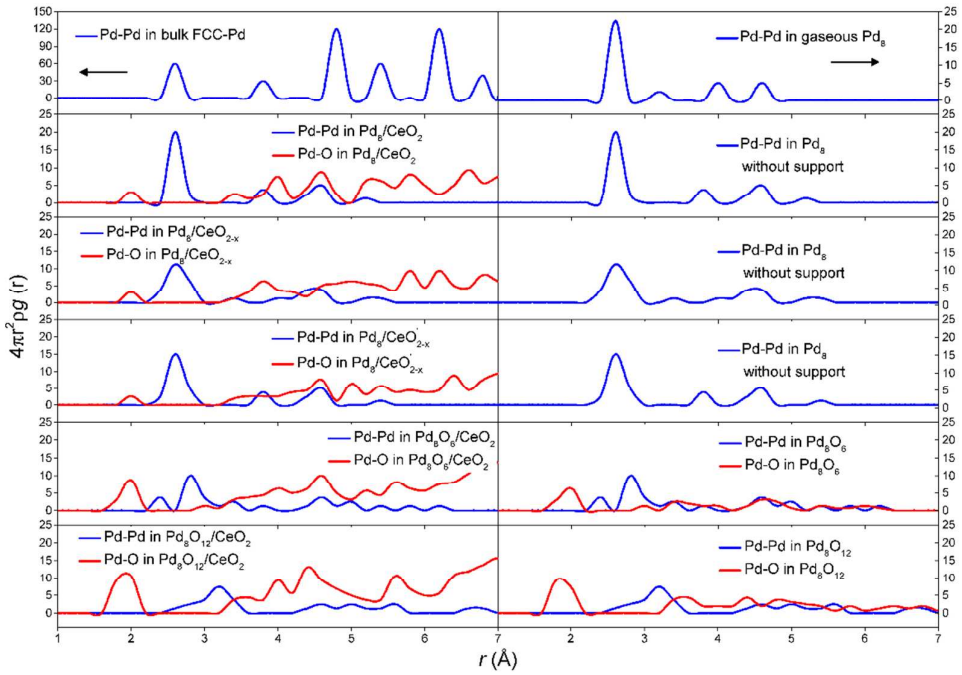

Figure S2. The calculated radial distribution functions of bulk Pd and $Pd_8(O_x)/CeO_2$.

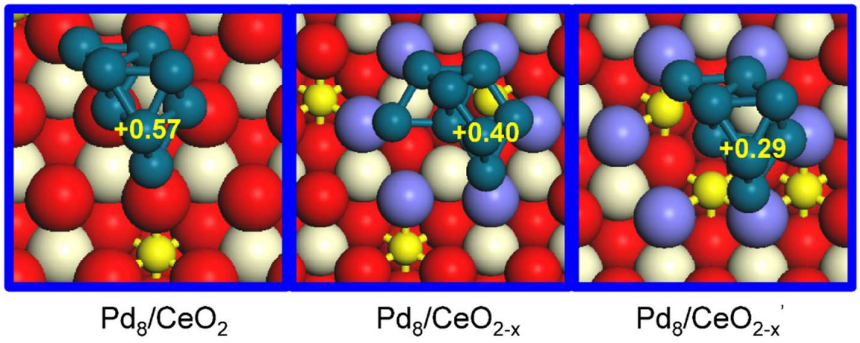

Figure S3. The positions of Ce^{3+} atoms and charge state of Pd_8 nanoparticles for Pd_8/CeO_2, Pd_8/CeO_{2-x} and Pd_8/CeO_{2-x}' structures. The yellow and small yellow spheres represent Ce^{4+} and Ce^{3+} atoms, respectively. The charge state of Pd_8 nanoparticles alculated by Bader charge analysis are indicated.

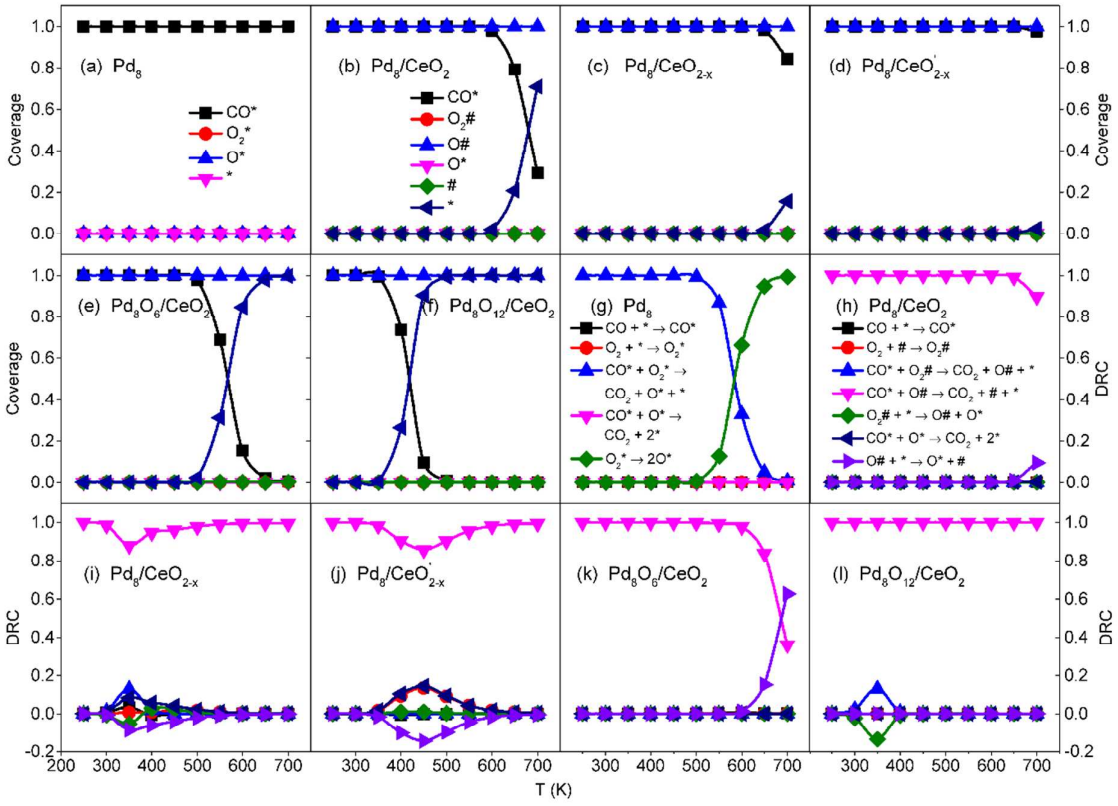

Figure S4. Calculated steady-state coverages (a) – (f) and DRC (g) – (l) analysis for CO oxidation on Pd_8 and CeO_2 supported $Pd_8(O_x)$ nanoclusters. Herein, * and # stand for the surface vacancies on $Pd_8(O_x)$ nanoparticle and CeO_2 support, respectively.

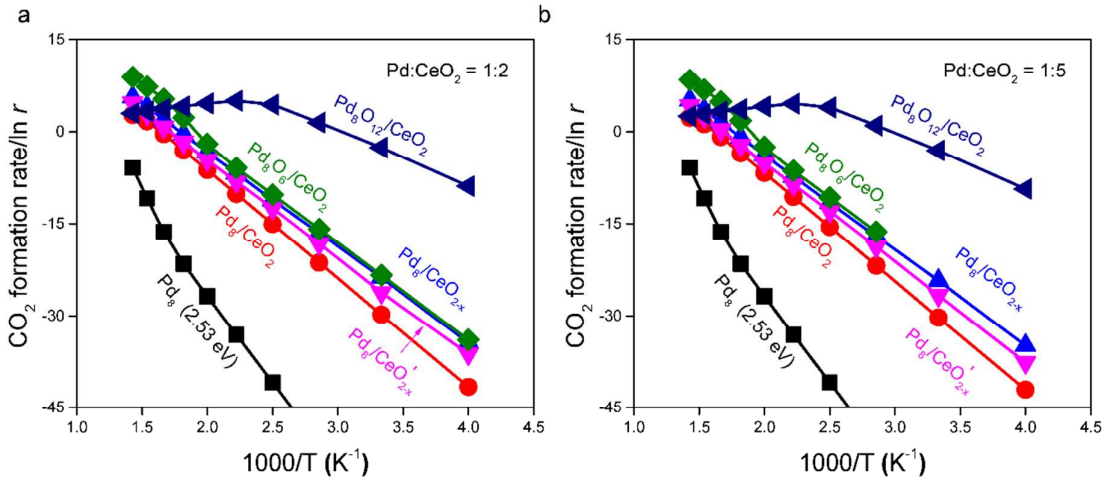

Figure S5. The calculated CO oxidation rate on various $Pd_8(O_x)/CeO_2$ catalysts with the variation of $Pd:CeO_2$ sites ratio. (a) $Pd:CeO_2$ = 1:2 and (b) $Pd:CeO_2$ = 1:5.

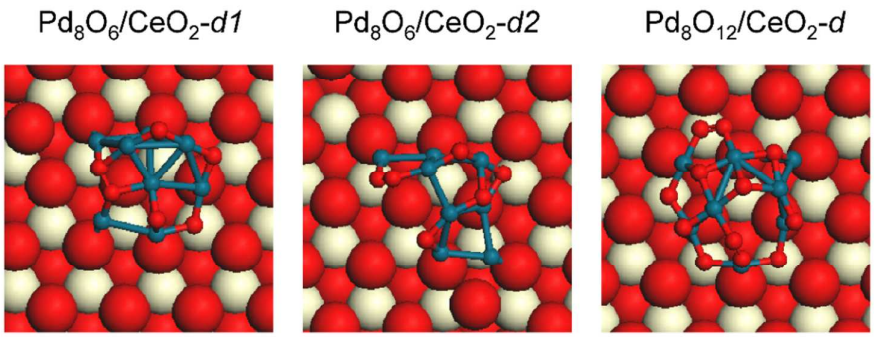

Figure S6. Three distorted Pd_8O_6/CeO_2-*d1,* Pd_8O_6/CeO_2-*d2* and Pd_8O_{12}/CeO_2-*d* structures generated in GCMC simulations which are considered to plot the scaling law.

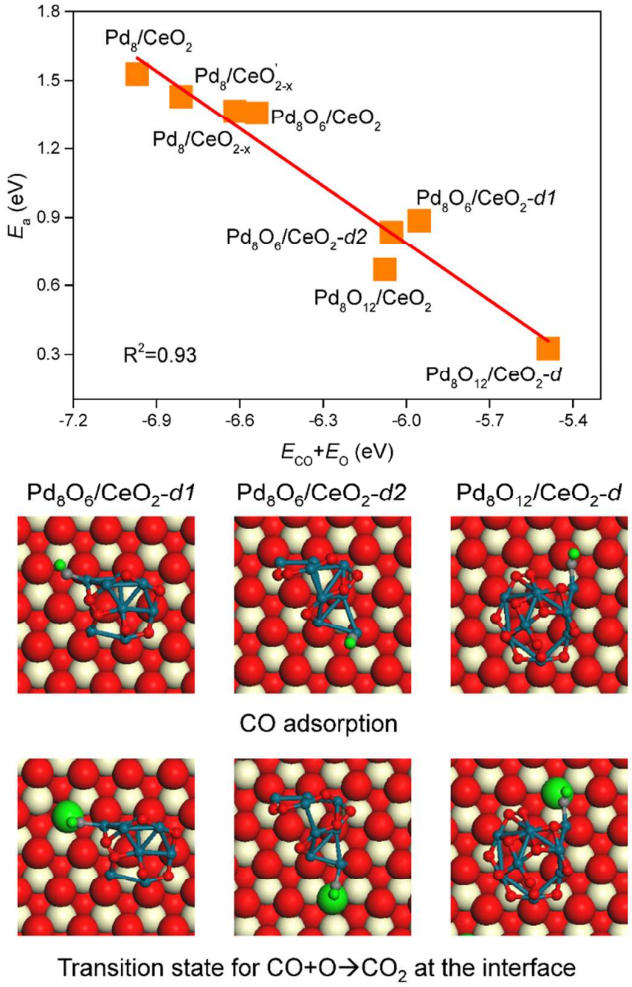

Figure S7. A linear scaling relationship between the reaction barriers of lattice oxygen vacancy formation and CO and O adsorption energies on $Pd_8(O_x)$ and CeO_2, respectively. The distorted two Pd_8O_6/CeO_2 structures and one Pd_8O_{12}/CeO_2 structure generated in corresponding GCMC simulations are considered. The configurations of CO adsorption and the transition state for CO+O→CO_2 reaction occurring at the interface of the three distorted structures are shown.

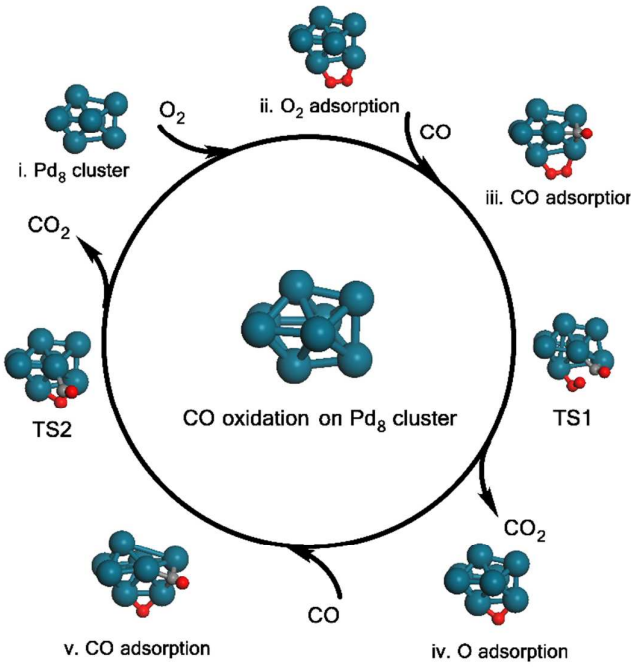

Figure S8. CO oxidation cycle without O_2 dissociation on Pd_8 nanoparticle.

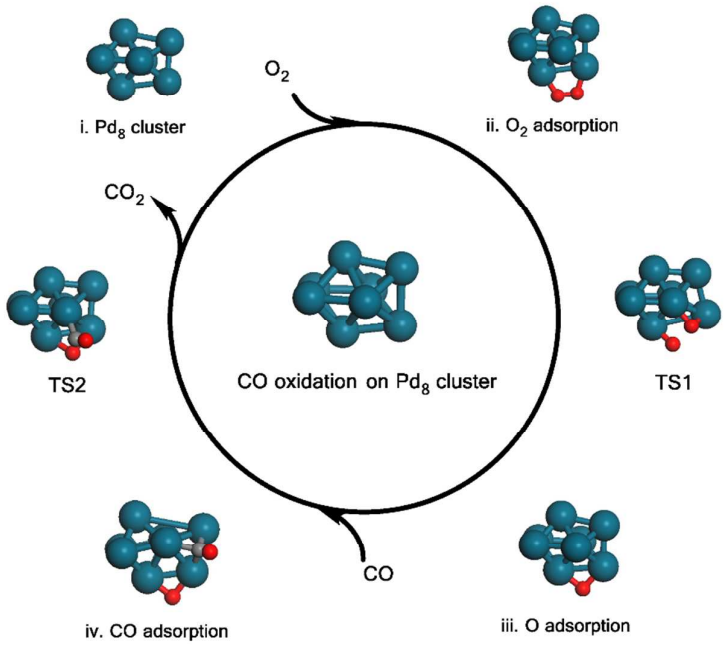

Figure S9. CO oxidation cycle via O_2 dissociation pathway on Pd_8 nanoparticle.

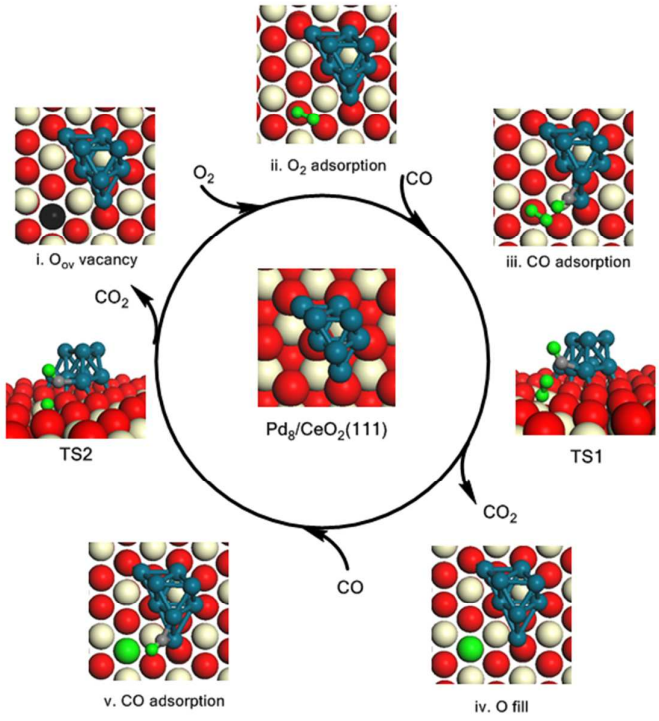

Figure S10. CO oxidation cycle without O_2 dissociation on Pd_8/CeO_2 structure. The green and grey spheres are O and C atoms involved in CO oxidation, respectively. This notation is used throughout this SI file.

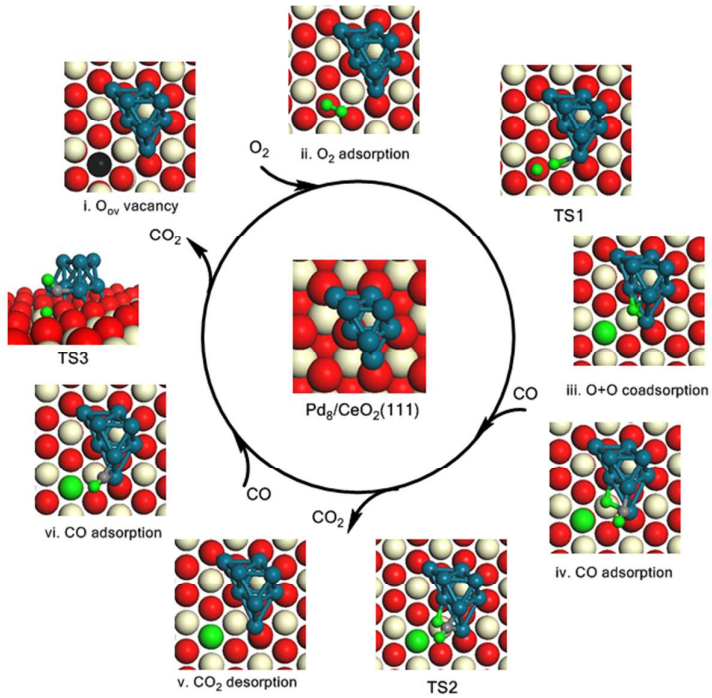

Figure S11. CO oxidation cycle via O_2 dissociation pathway on Pd_8/CeO_2 structure.

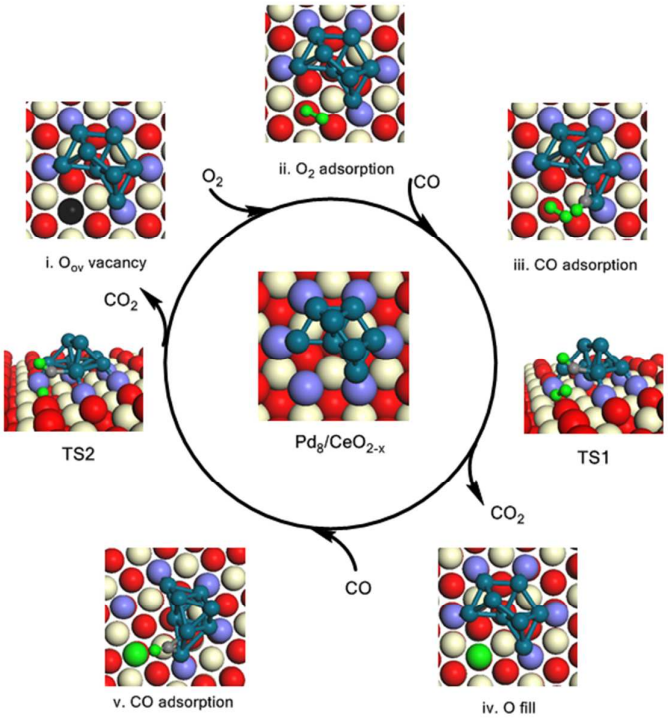

Figure S12. CO oxidation cycle without O_2 dissociation on Pd_8/CeO_{2-x} structure. The purple spheres are the O atoms around the oxygen vacancy site.

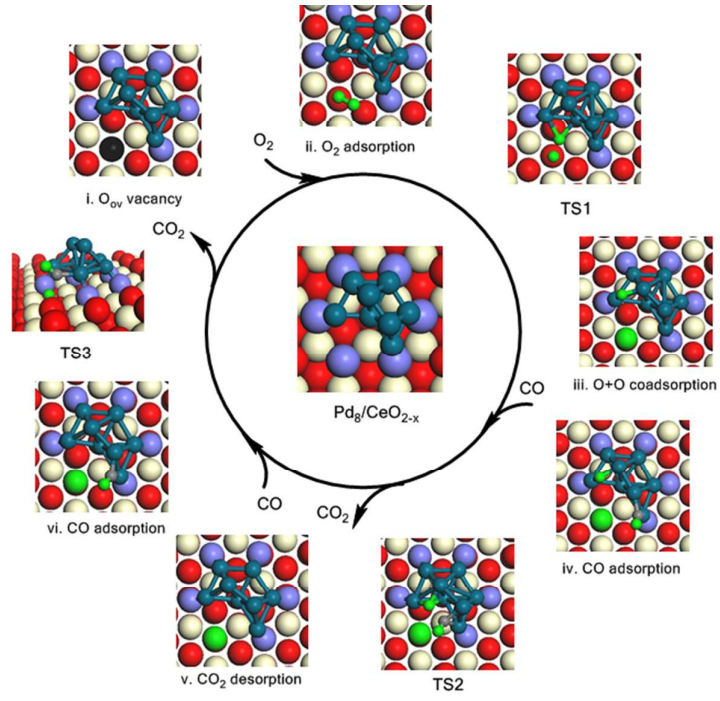

Figure S13. CO oxidation cycle via O_2 dissociation pathway on Pd_8/CeO_{2-x} structure.

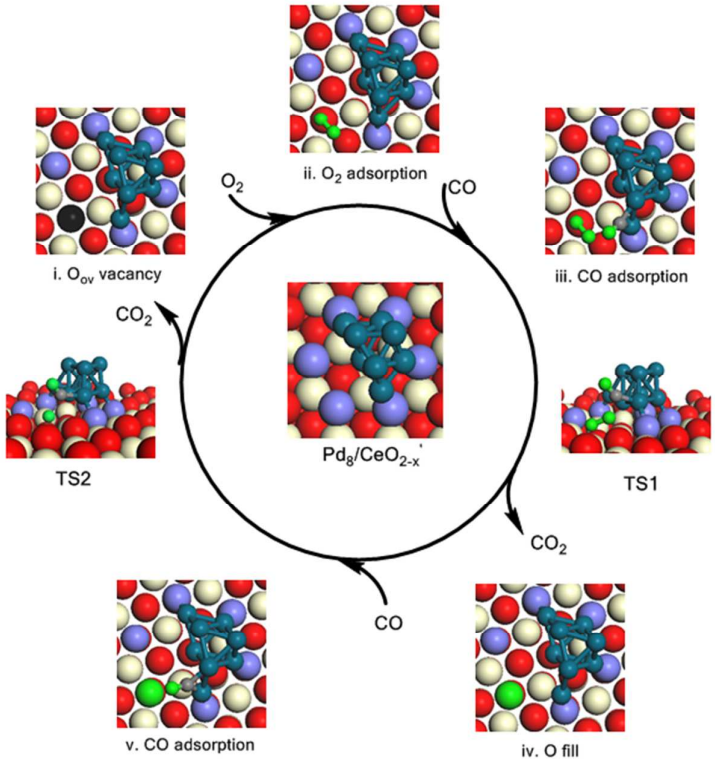

Figure S14. CO oxidation cycle without O_2 dissociation on Pd_8/CeO_{2-x}' structure.

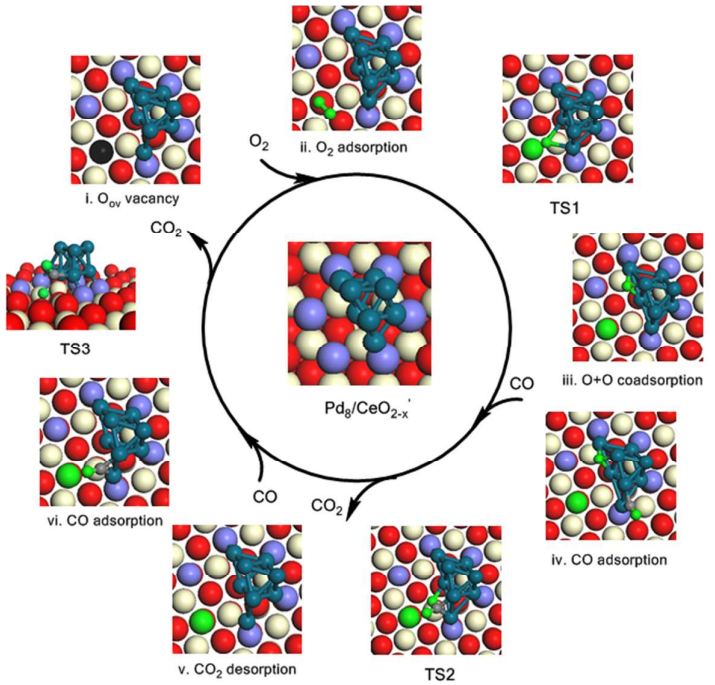

Figure S15. CO oxidation cycle via O_2 dissociation pathway on Pd_8/CeO_{2-x}' structure.

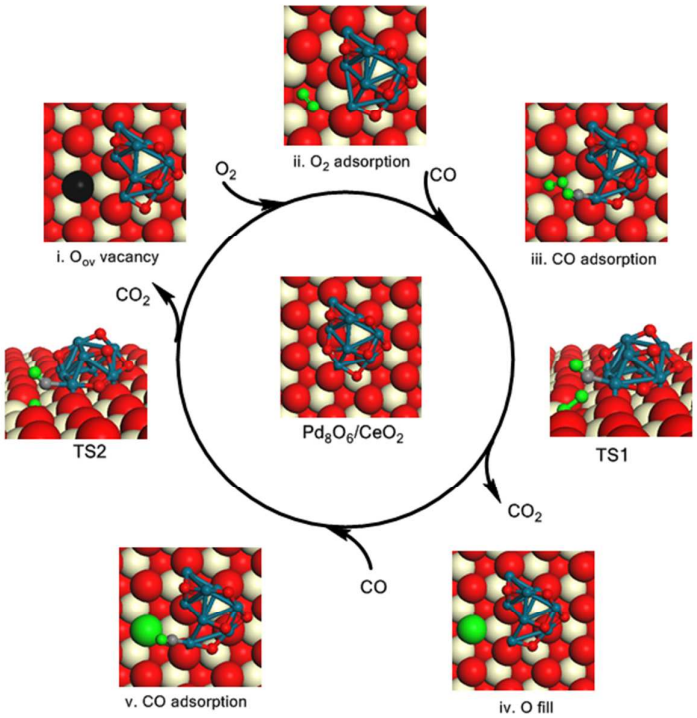

Figure S16. CO oxidation cycle without O_2 dissociation on Pd_8O_6/CeO_2 structure.

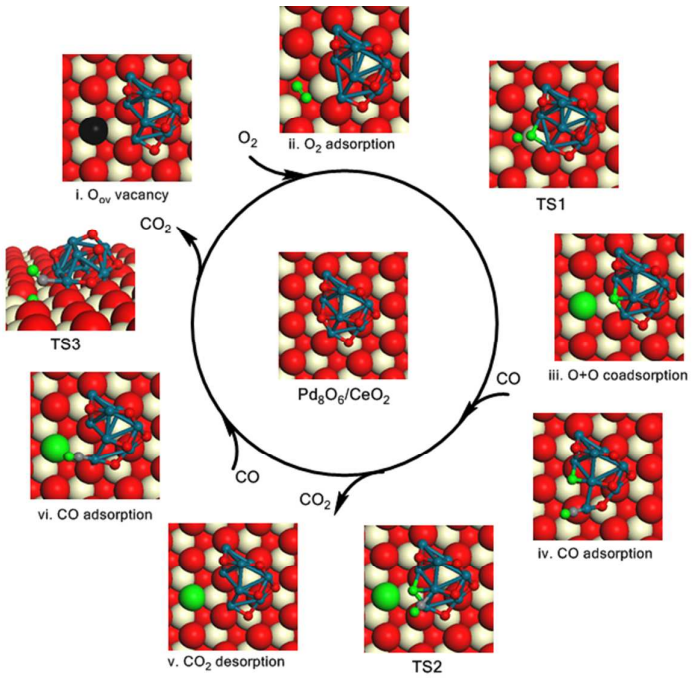

Figure S17. CO oxidation cycle via O_2 dissociation pathway on Pd_8O_6/CeO_2 structure.

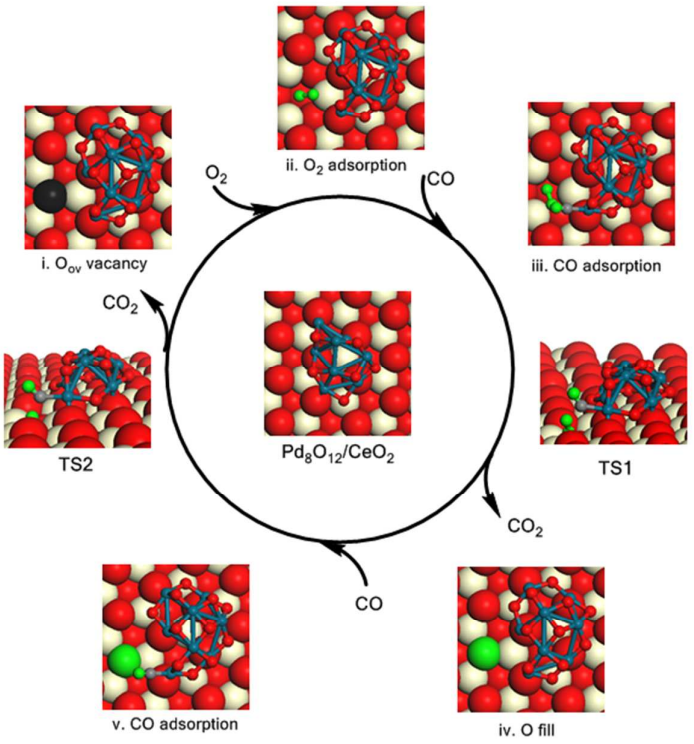

Figure S18. CO oxidation cycle without O_2 dissociation pathway on Pd_8O_{12}/CeO_2 structure.

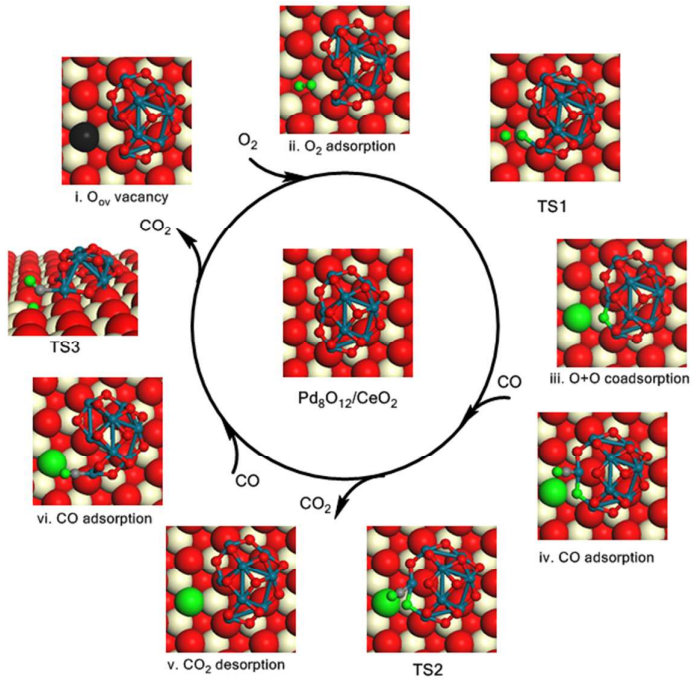

Figure S19. CO oxidation cycle via O_2 dissociation pathway on Pd_8O_{12}/CeO_2 structure.

References:

(1) G. Kresse; J. Hafner *Phys. Rev. B* **1993**, *47*, 558.
(2) G. Kresse; J. Furthmüller *Phys. Rev. B* **1996**, *54*, 11169.
(3) P. E. Blöchl *Phys. Rev. B* **1994**, *50*, 17953.
(4) J. P. Perdew; K. Burke; M. Ernzerhof *Phys. Rev. Lett.* **1996**, *77*, 3865.
(5) B. Hammer; L. B. Hansen; J. K. Nørskov *Phys. Rev. B* **1999**, *59*, 7413.
(6) C. Loschen; J. Carrasco; K. M. Neyman; F. Illas *Phys. Rev. B* **2007**, *75*, 035115.
(7) G. Henkelman; B. P. Uberuaga; H. Jónsson *J. Chem. Phys.* **2000**, *113*, 9901.
(8) G. Henkelman; H. Jónsson *J. Chem. Phys.* **2000**, *113*, 9978.
(9) L. B. Vilhelmsen; B. Hammer *J. Chem. Phys.* **2014**, *141*, 044711.
(10) D. Deaven; K. Ho *Phys. Rev. Lett.* **1995**, *75*, 288.
(11) D. Daven; N. Tit; J. Morris; K. Ho *Chem. Phys. Lett.* **1996**, *256*, 195.
(12) M. Chase Jr; C. Davies; J. Downey Jr; D. Frurip; R. McDonald; A. Syveraud *JANAF thermodynamic tables*; 3rd ed.; American Chemical Society/American Institute of Physics/National Bureau of Standards: Washington, DC, 1985.
(13) N. Metropolis; A. W. Rosenbluth; M. N. Rosenbluth; A. H. Teller; E. Teller *J. Chem. Phys.* **1953**, *21*, 1087.
(14) D. Frenkel; B. Smit *Understanding molecular simulation: from algorithms to applications*; Academic press, USA, 2001.
(15) H. Eyring *J. Chem. Phys.* **1935**, *3*, 107.
(16) P. Nitoń; A. Żywociński; M. Fiałkowski; R. Hołyst *Nanoscale* **2013**, *5*, 9732.
(17) I. A. W. Filot; R. A. van Santen; E. J. M. Hensen *Angew. Chem.* **2014**, *126*, 12960.
(18) I. A. Filot; R. J. Broos; J. P. van Rijn; G. J. van Heugten; R. A. van Santen; E. J. Hensen *ACS Catal.* **2015**, *5*, 5453.
(19) http://www.mkmcxx.nl/.
(20) M. Valden; X. Lai; D. W. Goodman *Science* **1998**, *281*, 1647.
(21) C. T. Campbell *Top. Catal.* **1994**, *1*, 353.
(22) C. T. Campbell *J. Catal.* **2001**, *204*, 520.
(23) C. Stegelmann; A. Andreasen; C. T. Campbell *J. Am. Chem. Soc.* **2009**, *131*, 8077.
(24) G. Li; L. Li; Y. Yuan; J. Shi; Y. Yuan; Y. Li; W. Zhao; J. Shi *Appl. Catal. B-Environ.* **2014**, *158*, 341.
(25) J. Wu; L. Zeng; D. Cheng; F. Chen; X. Zhan; J. Gong *Chin. J. Catal.* **2016**, *37*, 83.
(26) G. Spezzati; Y. Su; J. P. Hofmann; A. D. Benavidez; A. T. DeLaRiva; J. McCabe; A. K. Datye; E. J. Hensen *ACS Catal.* **2017**, *7*, 6887.